

# Unveiling the mechanism of phase and morphology selections during the devitrification of Al-Sm amorphous ribbon

Fanqiang Meng<sup>1,\*</sup>, Yang Sun<sup>2,†</sup>, Feng Zhang,<sup>3</sup> Bo Da,<sup>4</sup> Cai-Zhuang Wang,<sup>3</sup>  
Matthew J. Kramer<sup>3</sup>, Kai-Ming Ho,<sup>3</sup> and Dongbai Sun<sup>1,5,‡</sup>

<sup>1</sup>*Sino-French Institute of Nuclear Engineering and Technology, Sun Yat-Sen University, Zhuhai, Guangdong 519082, China*

<sup>2</sup>*Department of Applied Physics and Applied Mathematics, Columbia University, New York, New York 10027, USA*

<sup>3</sup>*Ames Laboratory, U.S. Department of Energy and Department of Physics, Iowa State University, Ames, Iowa 50011, USA*

<sup>4</sup>*Research and Services Division of Materials Data and Integrated System, National Institute for Materials Science, 1-1 Namiki, Tsukuba, Ibaraki 305-0044, Japan*

<sup>5</sup>*School of Materials Science and Engineering, Sun Yat-Sen University, Guangzhou 510275, China*



(Received 7 October 2020; accepted 1 April 2021; published 19 April 2021)

The complex interplay between energetic and kinetic factors that governs the phase and morphology selections can originate at the earliest stage of crystallization in the amorphous parent phases. Because of the extreme difficulties in capturing the microscopic nucleation process, a detailed picture of how initial disordered structures affect the transformation pathway remains unclear. Here, we report the experimental observation of widely varying phase selection and grain size evolution during the devitrification of a homogeneous melt-spun glassy ribbon. Two different crystalline phases  $\theta$ -Al<sub>5</sub>Sm and  $\varepsilon$ -Al<sub>60</sub>Sm<sub>11</sub> are found to form in the different regions of the same metallic glass (MG) ribbon during the devitrification. The grain size of the  $\varepsilon$ -Al<sub>60</sub>Sm<sub>11</sub> phase shows a strong spatial heterogeneity. The coarse-grained  $\varepsilon$ -Al<sub>60</sub>Sm<sub>11</sub> phase coupled with the small volume fraction of the  $\theta$ -Al<sub>5</sub>Sm phase is preferably formed close to the wheel side of the melt-spun ribbon. Combining experimental characterization and computational simulations, we show that phase selection and microstructure evolution can be traced back to different types and populations of atomic clusters that serve as precursors for the nucleation of different crystalline phases. Inhomogeneous cooling rates cause different structure orders across the glass sample during the quenching process. Our findings provide direct insight into the effect of structural order on the crystallization pathways during the devitrification of MG. It also opens an avenue to study the detailed nucleation process at the atomic level using the MG as a platform and suggests the opportunity of microstructure and property design via controlling the cooling process.

DOI: [10.1103/PhysRevMaterials.5.043402](https://doi.org/10.1103/PhysRevMaterials.5.043402)

## I. INTRODUCTION

Understanding crystallization pathways plays a key role in discovering and designing materials [1]. When a liquid is cooled slowly, phase selection typically follows the equilibrium phase diagram. With deeper undercooling, solidification rates increase, driving the system further from equilibrium. Under very high cooling rates, crystallization can be frustrated, and glass can form. Devitrification by reheating glass systems can have an asymmetric behavior in the phase selection compared with the crystallization by cooling from the liquid, emphasizing the complex competition between thermodynamics and kinetics [2,3]. Solidification or devitrification under far-from-equilibrium conditions can often lead to unexpected phase selection and microstructures [4–6], which is of vital importance in the design of materials with tailored structures and properties. Understanding its fundamental physics of transformation pathways by which different

microstructures evolve as a function of increasing departure from equilibrium is essential. However, observing the atomic-level process of nucleation from the very beginning of crystallization remains a long-time challenge [7–10].

As a representative far-from-equilibrium system, *glass*, sometimes thought of as a “frozen liquid” state [11], provides an ideal platform to investigate the correlation between pre-existing nuclei retained during the vitrification and the phase transformation pathway in the devitrification process. Even the structurally simplest metallic glass (MG) has shown a far richer-than-expected phase transformation behavior [12–14]. Phase selection during devitrification is not only affected by the thermodynamic driving force but also kinetic factors. Several scenarios were proposed to understand the crystallization of amorphous materials, e.g., phase separation [15–17] and diffusion-controlled nucleation [18]. Recent studies of atomic structure evidence that structural ordering can be quite abundant in the seemingly homogeneous liquids and glasses [19–23]. Local clusters from undercooled melts or amorphous alloys, such as icosahedral clusters [24,25], quenched-in nuclei [26,27], and short- and medium-range order [24,28], are believed to have an impact on subsequent crystallization and devitrification. It was proposed [27] that structural similarities

\*mengfq5@mail.sysu.edu.cn

†ys3339@columbia.edu

‡sundongbai@mail.sysu.edu.cn

between the crystalline phase and quenched-in nuclei can reduce the interfacial energy and, thus, promote polymorphic devitrification processes. Detailed analysis of theoretical models also indicates competing orders between the crystalline phase and liquids can impact crystal- and glass-forming behavior [29]. Therefore, it requires detailed information on structural orders in the initial liquid and glass states to understand the phase selection and microstructure in the subsequent crystallization and devitrification processes.

In this paper, we focus on Al-Sm MG, which has complex phase selections during devitrification. A small variation of Sm concentration can significantly alter the devitrification mechanisms of amorphous Al-Sm alloys, which varies from primary crystallization of nanoscaled  $\alpha$ -Al at 8 at. % Sm, polymorphic transformation at 10 at. % Sm, and eutectic crystallization for 12 at. % Sm [30]. Recent experiments coupled with computer simulations suggested the complex metastable phase selection in Al-Sm is dependent on chemical composition and the processing technique, such as melting spinning [14], magnetron sputtering [13], or solid-state amorphization [31]. The Al-Sm MG of melt-spun ribbon (MSR) can devitrify into the  $\varepsilon$ -Al<sub>60</sub>Sm<sub>11</sub> crystalline phase [14], while the  $\theta$ -Al<sub>5</sub>Sm phase was found to crystallize from the Al-Sm MG of sputtered thin film (STF) [13]. Computer simulations revealed that the devitrified crystalline phases exhibit similar atomic clusters with the undercooled Al-Sm liquids [32]. It was also found that the anisotropy of crystal growth of Al-Sm alloy has a strong correlation with atomic interfacial structures [33].

In this paper, we analyze the initial crystallization and the grain size of the phases devitrified from the binary Al-Sm glassy ribbon. We show a strong dependence of phase selection and morphology on the distance from the wheel side surface in the melt spinning. Coarse-grained  $\varepsilon$ -Al<sub>60</sub>Sm<sub>11</sub> coupled with a small volume fraction of  $\theta$ -Al<sub>5</sub>Sm phases are present close to the wheel side of the ribbon, where the highest cooling rate is achieved. Meanwhile, the  $\varepsilon$ -Al<sub>60</sub>Sm<sub>11</sub> phase with the smallest grain size locates around 5  $\mu$ m away from the wheel side. With the help of computer simulation, we rationalize the interdependence of the phase selection during devitrification and the local cooling rate during vitrification.

## II. METHOD

### A. Experimental procedures

Al-12.4 at. % Sm ingot was prepared by Materials Preparation Center (MPC, Ames Laboratory (USDOE) [34]) by arc melting 99.9% Sm and 99.99% Al in an argon atmosphere. Amorphous ribbons with an average thickness of  $\sim 20$   $\mu$ m were produced by a single copper block melt-spinner, quenching from 1373 K at a tangential wheel speed of 30 m/s. The ejection pressure used was  $120 \pm 1$  torr He over the base chamber pressure [35]. The amorphous nature of the ribbon was confirmed using transmission electron microscopy (TEM), lab-source x-ray diffraction (XRD, Bruker D8 Discover diffractometer with Cu target) and high-energy synchrotron x-ray scattering. The representative TEM image with corresponding selected area diffraction (SAD) and wide-angle x-ray scattering (WAXS) patterns shown in the Supplemental Material [36] reveals the only amorphous

phase without any crystal. The chemical composition of the MSR was measured using x-ray fluorescence (Bruker Tornado M4) and energy-dispersive x-ray spectroscopy (EDS) equipped on a scanning electronic microscope (FEI Teno Lovac). The crystallization behaviors of the as-spun amorphous ribbons were characterized using dynamic scanning calorimetry (DSC, Perkin Elmer Pyris 1) with a constant heating rate of 10 K/min.

The devitrification during isochronal heating was examined *in situ* using time-resolved high-energy x-ray diffraction, utilizing monochromatic x rays (energy of 71.77 keV, the wavelength of 0.01729 nm) at the sector 1-ID-E of Advanced Photon Source (APS) at Argonne National Laboratory operated by the U.S. Department of Energy. A two-stage forward-scattering detector configuration was used for simultaneous collection of WAXS and small-angle x-ray scattering (SAXS) signals. Samples used for WAXS-SAXS experiments were filled in a thin-walled SiO<sub>2</sub> capillary tube with 2 mm inner diameter and sealed in argon. For *in situ* heating, the capillary was placed in a tubular stainless-steel holder with a 5 mm x-ray pass window, which was heated using an infrared furnace. Two thermocouples were placed in contact with the capillary to record temperatures. The measured temperatures for the furnace used at APS were calibrated to the temperatures measured via DSC run using identical heating rates.

The microstructure evolution during devitrification was further probed using TEM and scanning transmission electron microscopy (STEM). Samples for TEM-STEM characterization were prepared using a dual-beam focused ion beam instrument (FEI Helios NanoLab G3 UC). The observations were carried out using Tecnai G<sup>2</sup> F20 and FEI Titan Themis 300 Cubes aberration-corrected instruments equipped with an EDS detector at an operation voltage of 200 kV.

### B. Computational methods

The long-time, large-scale molecular dynamics (MD) simulation was performed using the GPU-accelerated LAMMPS [37–39] code with a semi-empirical potential [40] in the Finnis–Sinclair form [41] for the energy calculations. The MG structures from this potential have demonstrated good agreement with the structure of Al<sub>90</sub>Sm<sub>10</sub> liquid determined from *ab initio* MD simulations and amorphous solids in experiments [32]. The constant number of atoms, pressure, and temperature (NPT) ensemble was applied with Nose–Hoover thermostats. The time step of the simulation was 2.5 fs. A sub- $T_g$  annealing technique [42] was employed to obtain the glass model with lower cooling rates. The initial liquid structure, containing 4500 Al atoms and 500 Sm atoms, were held at 2000 K for 2.5 ns to reach equilibrium. Then the liquid was continuously cooled down with a constant cooling rate of  $10^{10}$  K/s to 650 K, which is below the glass transition temperature  $T_g \sim 693$  K [40]. After that, the as-quenched structure was annealed isothermally at 650 K for up to 50  $\mu$ s, followed by a continuous cooling at  $10^{10}$  K/s to 300 K. Moreover, six other Al<sub>90</sub>Sm<sub>10</sub> glass models were generated using uniform continuous cooling from 2000 to 300 K with different cooling rates of  $10^{13}$ ,  $10^{12}$ ,  $10^{11}$ ,  $10^{10}$ ,  $10^9$ , and  $10^8$  K/s. The effective

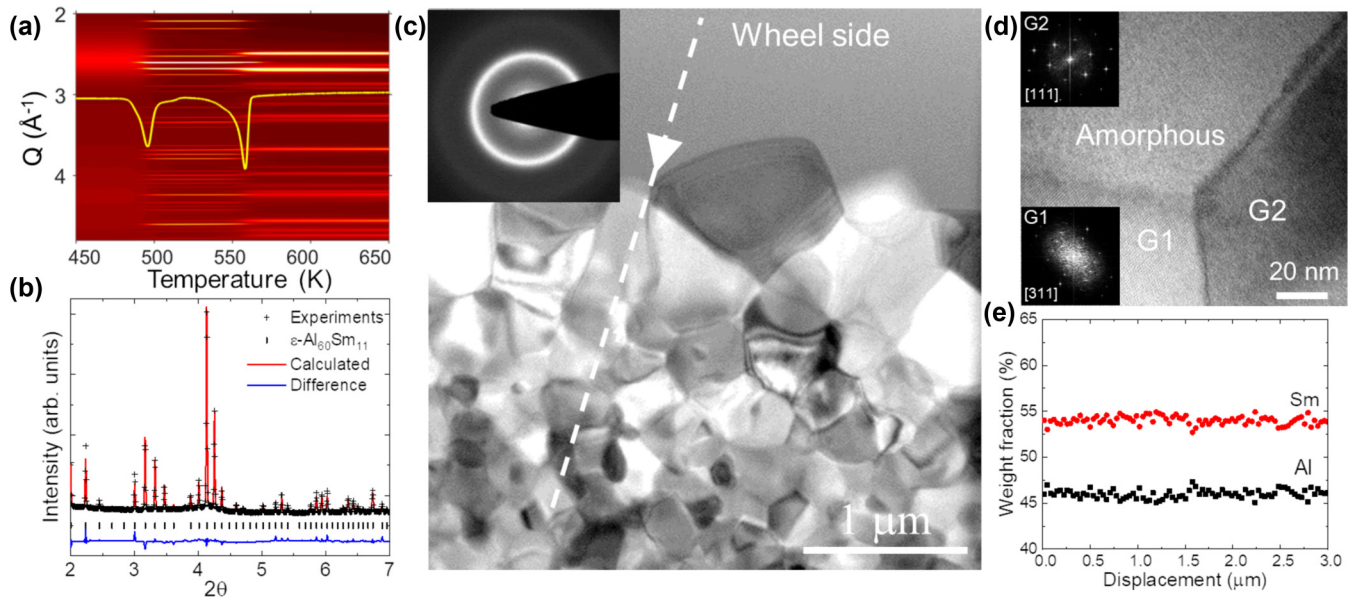


FIG. 1. Phase transformation and microstructure of Al-Sm metallic glass (MG) upon devitrification. (a) Accumulated wide-angle x-ray scattering (WAXS) patterns as a function of temperature with a constant heating rate of 10 °C/min and corresponding dynamic scanning calorimetry (DSC) curve. (b) General Structure Analysis System Rietveld result of WAXS pattern at a temperature of 500 K. (c) Bright-field (BF) transmission electron microscopy (TEM) images of melt-spun ribbon after heating to 500 K in the DSC. The selected area diffraction (SAD) pattern (inset) is obtained from the amorphous region close to the wheel side. The arrow indicates the direction away from the wheel side. (d) High-resolution (HR)-TEM image of the interface between  $\epsilon$ -Al<sub>60</sub>Sm<sub>11</sub> and amorphous phases; fast Fourier transform (FFT) patterns (inset) from two different grains. (e) Energy-dispersive x-ray spectroscopy (EDS) element profiles along the dashed line marked in (c).

cooling rate of the sub- $T_g$  annealed model was determined by the potential energy [43] as  $4 \times 10^7$  K/s.

### III. RESULTS AND DISCUSSION

#### A. Dependence of phase selection and microstructure on the distance to the wheel side

Figure 1(a) shows the crystallization behaviors monitored using DSC and *in situ* synchrotron WAXS at a constant heating rate of 10 K/min. A two-stage phase transformation can be seen from the contrast changes in the WAXS patterns accompanied by two exothermic peaks in the DSC profile. Rietveld analysis (General Structure Analysis System software) was carried out to confirm the phase transformation sequences and evolution of phase fraction (see Fig. S2 in Supplemental Material [36]). The first exothermic peak corresponds to the formation of the  $\epsilon$ -Al<sub>60</sub>Sm<sub>11</sub> phase, a cubic structure with a large unit cell containing 144 atoms and  $a = b = c = 1.39$  nm [14]. Continuous heating up to 538 K leads to the decomposition of  $\epsilon$ -Al<sub>60</sub>Sm<sub>11</sub> into  $\pi$ -Al<sub>5</sub>Sm and face-centered cubic (fcc)-Al (see Fig. S3 in Supplemental Material [36]). The representative Rietveld diffraction pattern at 500 K is shown in Fig. 1(b), in which all the peaks can be indexed by the  $\epsilon$ -Al<sub>60</sub>Sm<sub>11</sub> phase with partial occupancy. Meanwhile, a diffuse halo is present at  $2\theta = 4.2^\circ$  in Fig. 1(b), suggesting the presence of an amorphous phase. *Ex situ* TEM was employed to characterize the microstructural evolution. A bright-field TEM (BF-TEM) image of the ribbon heated at 10 K/min to 500 K and then cooled in a DSC furnace is shown in Fig. 1(c). Well-defined grains with sizes varying by several hundred nanometers are observed in the region away from the wheel side surface. In contrast, the part closer

to the wheel side surface appears to be still in amorphous nature, which is confirmed by the SAD [inset of Fig. 1(c)] pattern, consistent with the WAXS result. A clear interface between amorphous and  $\epsilon$ -Al<sub>60</sub>Sm<sub>11</sub> phases can be observed in the high-resolution (HR) TEM image shown in Fig. 1(d), suggesting the crystallization is not initiated close to the wheel side. The absence of nano-sized fcc-Al inside current  $\epsilon$ -Al<sub>60</sub>Sm<sub>11</sub> grains is different from the previously observed mixture of fcc-Al and  $\epsilon$ -Al<sub>60</sub>Sm<sub>11</sub> structures devitrified from Al-Sm MG with lower Sm concentrations [44,45]. It indicates the current devitrification may be in a partitionless manner. To further confirm its chemical homogeneity, the chemical composition was examined using EDS measurement along the line indicated in Fig. 1(c). Indeed, Fig. 1(e) shows the measured Al-Sm concentrations from the retained amorphous layer to crystalline grains do not present any chemical variation. Therefore, the crystallization from the current Al-Sm MG near the spinning wheel side has a spatial inhomogeneity with the coexistence of multiple  $\epsilon$ -Al<sub>60</sub>Sm<sub>11</sub> grains and is amorphous, meanwhile showing a chemical homogeneity.

To further elucidate the crystallization behavior of the Al-Sm MSR, the devitrified sample was isothermally annealed at elevated 508 K for 720 s to characterize the morphology of crystallized phases. A representative TEM micrograph of the structure near the wheel side after isothermal annealing is shown in Fig. 2(a). The amorphous layer close to the wheel side [Fig. 1(c)] no longer presents after the extended annealing at the elevated temperature. Instead, the structure becomes elongated and coarsely grained, which then transit to finer grains with increasing distance from the wheel side surface. SAD patterns (not shown) for the grains demonstrate that most of the elongated grains are  $\epsilon$ -Al<sub>60</sub>Sm<sub>11</sub> phase, except the



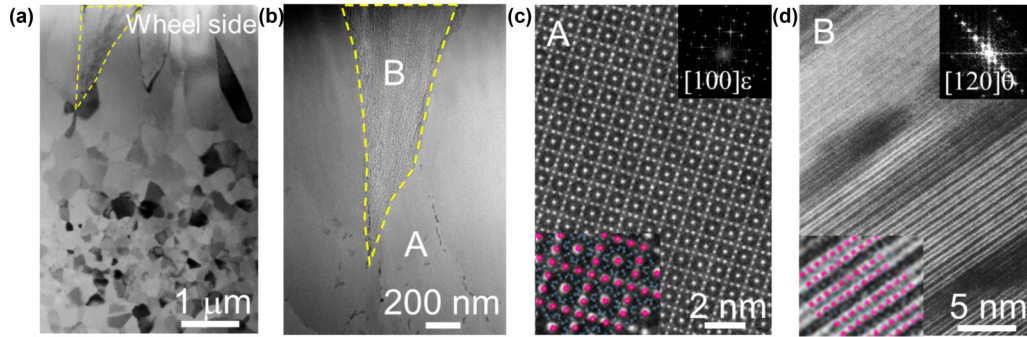


FIG. 2. Dependence of phase selection on the distance from the wheel side of a fully crystallized sample. (a) Bright-field (BF) transmission electron microscopy (TEM) images of melt-spun ribbon (MSR) annealed at 508 K for 720 s. The arrow indicates the direction away from the wheel side. (b) High-angle annular dark-field (HAADF) scanning TEM (STEM) images of the region marked by the dashed line in (a). (c) and (d) High-resolution HAADF-STEM images of  $\epsilon$ -Al<sub>60</sub>Sm<sub>11</sub> and  $\theta$ -Al<sub>5</sub>Sm phases corresponding to A and B regions in (b), respectively. The insets are fast Fourier transform (FFT) pattern and superposed atomic structures with the patterns where red dots represent Sm, and blue dots are Al.

region marked by the dashed line in Fig. 2(a). The high-angle annular dark-field (HAADF) STEM image of the area close to the wheel side at higher magnification is shown in Fig. 2(b), in which the chemical composition contrast is present, suggesting a multiphase configuration. The HR-HAADF-STEM image and corresponding fast Fourier transform (FFT) patterns of regions A and B are shown in Figs. 2(c) and 2(d), respectively. Figure 2(c) shows the atomic structure in the  $\epsilon$ -Al<sub>60</sub>Sm<sub>11</sub> phase along with a superimposed schematic of the atomic packing. Due to the large Z contrast between Al and Sm atoms, Al sites are almost not visible in HAADF-STEM mode. The bright dots are mainly caused by the Sm sites [46], which is consistent with the lattices shown in the inset of Figs. 2(c) and 2(d). The atomic packing in the B region [Fig. 2(d)] exhibits another structural pattern that corresponds to the  $\theta$ -Al<sub>5</sub>Sm phase, which was observed only from Al-Sm STF previously [13]. The dark contrast in Fig. 2(d) is confirmed to be the fcc-Al distributed along the  $\langle 001 \rangle$  direction of  $\theta$ -Al<sub>5</sub>Sm phase using HR-TEM.

Not only is the phase selection dependent on relative distance from the wheel side surface, but the morphology of  $\epsilon$ -Al<sub>60</sub>Sm<sub>11</sub> grains is also dependent on this distance, as can be seen in Figs. 1(c) and 2(a). The evolution of grain size as a distance from the wheel side was further examined by isothermally annealing a sample at different temperatures and times. The microstructure of the sample annealed at 478 K for 660 s is shown in Fig. 3(a). Some amorphous regions are still retained in the area closest to the wheel side for this sample. In Fig. 3(b), the grain sizes of the  $\epsilon$ -Al<sub>60</sub>Sm<sub>11</sub> phase are measured as a function of distance from the wheel side for samples annealed at both 478 K for 660 s (partial crystallized) and 508 K for 720 s (fully crystallized) using the liner intercept method. Two independent samples were annealed at 478 K for 660 s to confirm the consistency in measurements. The grain size of the  $\epsilon$ -Al<sub>60</sub>Sm<sub>11</sub> phase is larger at the region closest to the wheel side and decreases with the increasing distance from the wheel side until reaching a minimum at  $\sim 4$ – $5.5 \mu\text{m}$  away from the wheel side. With further increasing distance from the wheel side, the grain size increases again. Three samples show a very consistent trend of the grain size change as a function of distance from wheel sides.

Current experiments show the phase selection and microstructural evolution during the devitrification of the Al-Sm MSR with a strong dependence on the distance from the wheel side surface. Figure 1 indicates an inhomogeneous nuclei density of  $\epsilon$ -Al<sub>60</sub>Sm<sub>11</sub> phase from the wheel side to the free side in the MSR sample. This phenomenon should be attributed to the fact that the local cooling rate during the melt spinning varies significantly with the distance to the wheel

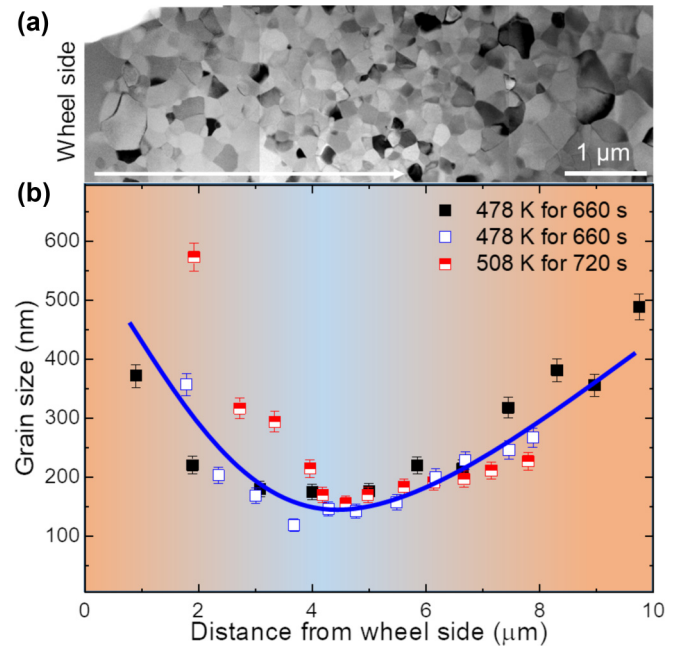


FIG. 3. Dependence of grain size on the distance from wheel side to free side. (a) Bright-field (BF) transmission electron microscopy (TEM) images of melt-spun ribbon (MSR) sample annealed at 478 K for 660 s, in which minor amorphous phase is retained close to the wheel side. The arrow indicates the direction away from the wheel side. (b) Grain size as a function of distance to wheel side surface in three samples: two samples were partially crystallized at 478 K for 660 s, and one sample was fully crystallized at 508 K for 720 s; blue curve is a guide to the eye.

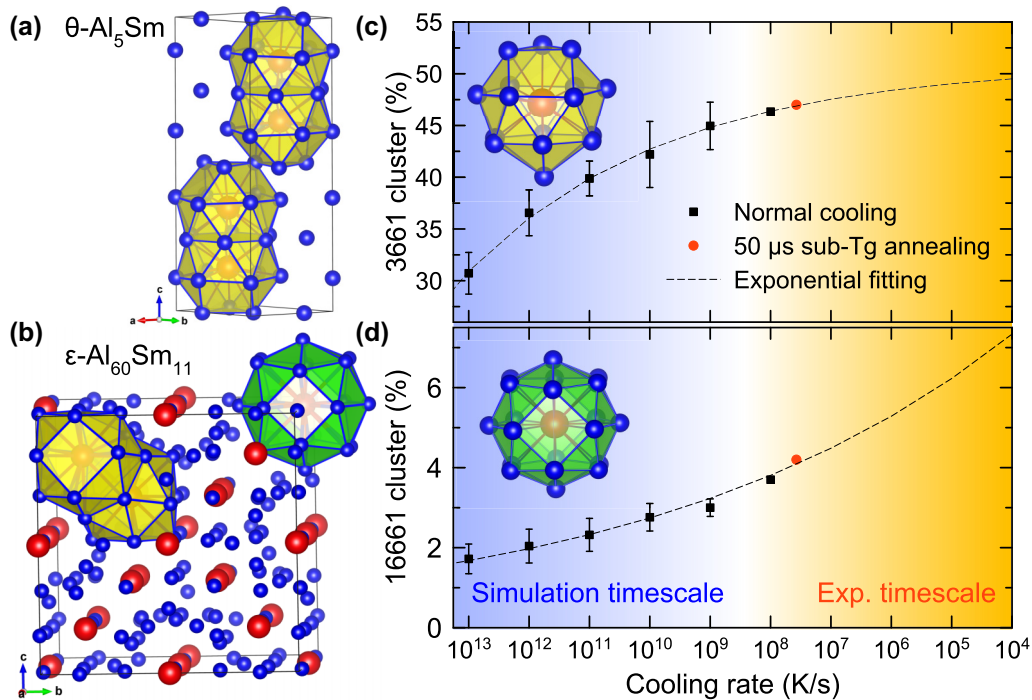


FIG. 4. The population of crystalline clusters as a function of cooling rates. Crystal structures of (a)  $\theta$ -Al<sub>5</sub>Sm and (b)  $\epsilon$ -Al<sub>60</sub>Sm<sub>11</sub>. The 3661 and 16661-type clusters are highlighted with yellow and green, respectively. Red is Sm, and blue is Al. The population of (c) 3661- and (d) 16661-type clusters as a function of cooling rates. The inserts in the upper and lower panel show the 3661 and 16661 clusters, respectively. The dashed line indicates the exponential fittings.

side surface. Melts that are first spun to the wheel side surface should suffer the fastest cooling. Indeed, numerical modeling [47,48] suggests the cooling rate close to the wheel side at 30 m/s can reach  $10^6$  K/s and decreases to  $10^4$  K/s at  $\sim 10$   $\mu$ m away from the wheel side, which is in good agreement with estimated values obtained by direct measurement in Al-Si [49] and Fe-Si-B systems [35]. Further strong evidence to support the inhomogeneous local cooling rate during melt spinning is the appearance of  $\theta$ -Al<sub>5</sub>Sm at the wheel side in Fig. 2. This phase was only observed from the Al-Sm STF samples before [13], which was prepared by condensation of metallic vapor through magnetron sputtering. The MG of STF should undergo a much higher cooling rate (estimated as  $\sim 10^9$  K/s [50]) than the averaged cooling rate in melt spinning. Therefore, the formation of  $\theta$ -Al<sub>5</sub>Sm at the wheel side in the current MSR and previous magnetron STF suggests the  $\theta$ -Al<sub>5</sub>Sm phase is favored during devitrification of the Al-Sm amorphous ribbon prepared using a higher cooling rate.

### B. Crystalline precursors in MG based on MD simulations

The observed difference of devitrification between wheel and free side of MSR demonstrates that the cooling rate can tune the phase selection and crystallization pathway of Al-Sm MG from  $\epsilon$ -Al<sub>60</sub>Sm<sub>11</sub> to  $\theta$ -Al<sub>5</sub>Sm. To further understand this scenario, MD simulations were performed to investigate the precursor population change with cooling rates in the MG samples. While  $\epsilon$ -Al<sub>60</sub>Sm<sub>11</sub> and  $\theta$ -Al<sub>5</sub>Sm phases have very different crystallographic features, one can see similarities from atomic clusters. As shown in Figs. 4(a) and 4(b), all Sm atoms in  $\theta$ -Al<sub>5</sub>Sm show the adjacent “3661”-type clusters,

which consist of a top triangular Al layer followed by two hexagonal Al layers and a bottom atom [see inset in Fig. 4(c)]. Here,  $\epsilon$ -Al<sub>60</sub>Sm<sub>11</sub> not only has 3661-type clusters but also presents a 16661-type cluster [inset in Fig. 4(d)], which consists of 20 Al coordinates, forming three hexagonal Al layers with two Al atoms at the top and bottom. The packing of these clusters fills three-dimensional space in the two crystalline phases (see Fig. S4 in Supplemental Material [36]). The fact that 16661 clusters only present in  $\epsilon$ -Al<sub>60</sub>Sm<sub>11</sub> indicates that the 16661 clusters should be the critical precursor to control the phase selection between  $\epsilon$ -Al<sub>60</sub>Sm<sub>11</sub> and  $\theta$ -Al<sub>5</sub>Sm.

To understand the dependence of the 3661 and 16661 clusters on the cooling rate in the Al<sub>90</sub>Sm<sub>10</sub> MG, we generated an MG model with uniform cooling experimental up to  $10^8$  K/s [51]. To reduce the gap between experimental and computational cooling rates, annealing simulation at a temperature below but close to the glass transition temperature (sub- $T_g$ ) was performed to achieve a more realistic atomistic MG model [42]. Thus, in addition to standard uniform cooling, sub- $T_g$  annealing was performed to reach an effective cooling rate of about  $4 \times 10^7$  K/s. With cluster alignment methods [52], the population of two types of clusters is shown as a function of the cooling rate in Figs. 4(c) and 4(d). The population of 3661 and 16661 clusters in the sub- $T_g$  annealed sample are consistent with the dashed line trend established based on the uniformly cooled samples. Overall, the MD simulations show that the 3661-type cluster is dominant in the MG sample, while 16661 only shows a small population. When slowing down the cooling rate, the population of 3661 clusters starts to show a plateau, while the 16661-cluster population shows a large increase. Therefore, the main effect of slower

cooling is to increase the 16661-cluster population. Since 16661 only exists in  $\varepsilon\text{-Al}_{60}\text{Sm}_{11}$ , the population of 16661 clusters is the rate-limiting factor controlling the formation of the  $\varepsilon\text{-Al}_{60}\text{Sm}_{11}$  under the slower cooling.

From the viewpoint of atomic packing, as shown in Fig. 4, the 16661 cluster is composed of 20 neighbor atoms surrounding the center Sm atom, while 3661 has 16 neighbor atoms. Because the averaged Sm coordination number in the  $\text{Al}_{90}\text{Sm}_{10}$  is  $\sim 16$ , 16661 is much rarer than 3661 in the glass and requires a much slower cooling rate to accumulate. Since 3661 clusters are always abundant in the glass regardless of cooling rates,  $\theta\text{-Al}_5\text{Sm}$  can form even when the glass was cooled at a higher cooling rate and not well relaxed. Therefore,  $\theta\text{-Al}_5\text{Sm}$  is observed in the STF and wheel side of MSR. However,  $\varepsilon\text{-Al}_{60}\text{Sm}_{11}$  is unlikely to form unless the population of 16661 clusters reaches a critical value at a sufficiently slow cooling rate. These analyses demonstrate that the population of 16661 clusters, controlled by the cooling rate, directly affects the phase selection of the Al-Sm MG in the devitrification.

The current observation can also be understood from the viewpoint of the temperature-time-transformation (TTT) diagram, which provides a framework to quantify the glass formation and crystallization. In a typical TTT diagram, at high cooling rates, the temperature-time trajectory cannot intersect the nose of the crystalline region (C-curve) so that it avoids the formation of the equilibrium crystalline phase and leads to a glass state. A recent study by Derlet and Maaß [53] revealed an isotherm relaxation could drive the model binary glass toward amorphous crystalline nanocomposite microstructures, which locates in-between the monolithic glass state and equilibrium crystalline state on the TTT diagram. Our current observation of cooling-rate-dependent glass structure and devitrification pathways supports the existence of such intermediate amorphous states in the TTT diagram. Depending on the distance of temperature-time curve away from the nose point, different short- or medium-range order could develop in the undercooling liquid or glass. These orderings eventually affect the devitrified phases and microstructures. Our findings further indicate the cooling process can greatly affect the intermediate states and their phase selection along the isotherm.

The shear stress between the supercooled liquid and rotating wheels is also an important factor to control the crystallization during the rapid quenching. Mura and Zaccone [54] reported that the flow-induced nucleus straining lowers the nucleation rate by increasing the nucleation energy barrier. This mechanism could further reduce the nucleus at the wheel side. Therefore, the high cooling rate and shear stress at the wheel side both can stabilize the glass structures against devitrification.

### C. Dependence of grain size on the distance to the wheel side

After understanding the cooling rate dependence of 16661 populations, we discuss the grain size profile of the  $\varepsilon\text{-Al}_{60}\text{Sm}_{11}$  phase observed in Fig. 3(b). In the current MG sample, the cooling rate is believed to be monotonously decreasing with the distance away from the wheel side, which directly correlates with the population of quenched-in 16661 nuclei [27].

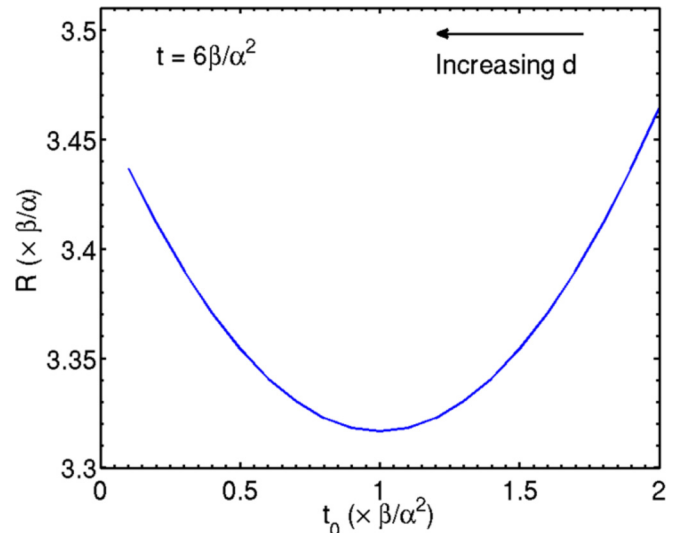


FIG. 5. Grain size at  $t = 6\beta/\alpha^2$  as a function of  $t_0$  according to the crystal growth model. The arrow indicates the direction of increasing distance ( $d$ ) from the wheel side.

Since a slower cooling rate leads to more 16661 clusters, as shown in Fig. 4(d), the number of  $\varepsilon\text{-Al}_{60}\text{Sm}_{11}$  nuclei should increase from the wheel side region to the free side. Interestingly, the measured grain size given in Fig. 3(b) shows a nonmonotonic dependence on the distance from the wheel side. This can be interpreted qualitatively by two kinetics at different stages of crystal growth. In the following, we set up a simplified model that captures the essential physics during the two stages of the growth, namely, free expansion and coalescence, and demonstrate that, through the competition of the different kinetics in these two growth stages, it is possible to produce the nonmonotonic grain size profile as observed in the experiments. During the early stage when a nucleus is fully embedded in the parent amorphous phase, the growth kinetics is controlled by the difference between the attachment and detachment rates at the interface [55], which results in a linear growth rate  $\alpha$ :  $dR/dt = \alpha$ , where  $R$  is the average nuclei radius. During the second stage, when nuclei impinge on each other, the crystal growth is controlled by the migration through curvature-driven grain boundary motion [56]. Both Monte Carlo simulations based on the Potts model and phase-field modeling [57] demonstrated that parabolic growth law ( $R^2 \sim t$ ) is satisfied in this scenario, or in the differential form:  $dR/dt = \beta/R$ , where  $\beta$  is a constant. We constructed the following model that captures the essence of the different kinetics in these two stages. That is, we assume the linear growth dominates when  $t < t_0$ , while the grain-boundary migration takes over when  $t > t_0$ . The rate equation for nuclei growth can then be written as

$$\frac{dR}{dt} = \begin{cases} \alpha & (t < t_0) \\ \beta/R & (t \geq t_0) \end{cases} \quad (1)$$

Since the two parameters controlling the growth kinetics  $\alpha$  and  $\beta$  have dimensions of  $[\text{length}][\text{time}]^{-1}$  and  $[\text{length}]^2[\text{time}]^{-1}$ , respectively,  $\beta/\alpha$  and  $\beta/\alpha^2$  give characteristic units for length and time, respectively. Assuming the grain-size measurement was taken well after  $t_0$  for all regions



across the sample, we plot the grain size at an arbitrary time instant  $t = 6\beta/\alpha^2$  as a function of  $t_0$  ranging from 0 to  $2\beta/\alpha^2$  in Fig. 5. As one can see, relatively large grains appear at both ends for different reasons: for large  $t_0$ , grains can experience unhindered growth in the amorphous background for a long period of time, while for small  $t_0$ , grains coalesce at relatively small sizes with high coalescence rates ( $\propto 1/R$ ). Clearly, the larger the nuclei density is, the shorter time it takes for nuclei to interact, so one expects  $t_0$  to decrease from the wheel side to the free side along the sample. Therefore, the model given in Eq. (1) provides a qualitative match with the experimental measurements, as shown in Fig. 3(b). We note, while the current model provides qualitative explanation on the grain size, a more sophisticated model which includes all the effects of cooling rate dependence and shear stress during the cooling process is still desired. We leave this for future study.

#### IV. CONCLUSIONS

In summary, the devitrification process of Al-Sm MG synthesized by melt spinning were systematically investigated using *in situ* synchrotron x-ray scattering, associated with *ex situ* TEM observations. *Ex situ* microstructure observation reveals that the thin layer close to the wheel side shows a delayed crystallization and dramatically different phase selection and morphology compared with the area far from the wheel side. MD simulations quantitatively show the cooling rate dependence of nuclei density in amorphous states. It suggests the 16661 nuclei are the key factor in determining phase selection between  $\varepsilon$ -Al<sub>60</sub>Sm<sub>11</sub> and  $\theta$ -Al<sub>5</sub>Sm. Cooling rate varying from the wheel to free side determines the density of quenched-in  $\varepsilon$ -Al<sub>60</sub>Sm<sub>11</sub> nuclei, thus resulting in a different grain size evolution. These results suggest that the cooling rate can be an important processing condition to control the structure of the seemingly homogeneous MG and its crys-

tallization pathways upon heating. Grain coalescence away from the wheel side is regarded as the origin for coarse grain size, while fewer nucleation sites close to the wheel side are the major factors to determine the overall grain morphology. These findings provide direct proof to support the hereditary dependence of crystallization behavior on the liquid and glass states. The results emphasize the key factor of the cooling rate on determining the phase and microstructure evolution during the devitrification process. It indicates the local chemical and structural order can be sensitive to the processing and can greatly affect the properties of an alloy, which can be quite general in many MG systems. Therefore, our findings could help develop the strategy of microstructure design via quenched-in clusters with controlling the cooling process.

#### ACKNOWLEDGMENTS

F.M. thanks R. T. Ott and M. F. Besser (Ames Laboratory, Iowa State University) for their support in the enlightening discussion. Work at Ames Laboratory was supported by the U.S. Department of Energy, Office of Science, Basic Energy Sciences, Division of Materials Science and Engineering under Contract No. DE-AC02-07CH11358. The use of the Advanced Photon Source was supported by the U.S. Department of Energy, Office of Science, Office of Basic Energy Sciences, under Contract No. DE-AC02-06CH11357. D.S. acknowledges support from “The Pearl River Talent Program.” F.M. acknowledges support from National Key Research and Development program (2020YFC2200503). Y.S. acknowledges the support from National Science Foundation awards EAR-1918126 and partial support from the Department of Energy Theoretical Chemistry Program through Grant No. DE-SC0019759. K.-M.H. acknowledges the support from National Science Foundation awards EAR-1918134.

- 
- [1] K. F. Kelton, F. Kenneth, and A. L. Greer, *Pergamon Materials Series* **15**, iii (2010).
  - [2] M. Wang, K. Zhang, Z. Li, Y. Liu, J. Schroers, M. D. Shattuck, and C. S. O’hern, *Phys. Rev. E* **91**, 032309 (2015).
  - [3] S. Lan, Z. Wu, X. Wei, J. Zhou, Z. P. Lu, J. Neufeind, and X. Wang, *Acta Mater.* **149**, 108 (2018).
  - [4] K. F. Kelton, *Phys. Rev. B* **45**, 75 (1991).
  - [5] F. Q. Meng, S. H. Zhou, R. T. Ott, M. J. Kramer, and R. E. Napolitano, *Materialia* **9**, 100595 (2020).
  - [6] N. Wang, Y. E. Kalay, and R. Trivedi, *Acta Mater.* **59**, 6604 (2011).
  - [7] J. Zhou, Y. Yang, Y. Yang, D. Kim, A. Yuan, X. Tian, C. Ophus, F. Sun, A. K. Schmid, and M. Nathanson, *Nature* **570**, 500 (2019).
  - [8] Z. Wang, F. Wang, Y. Peng, and Y. Han, *Nat. Commun.* **6**, 6942 (2015).
  - [9] D. Gebauer, A. Volkel, and H. Colfen, *Science* **322**, 1819 (2008).
  - [10] D. Gebauer, M. Kellermeier, J. D. Gale, L. Bergstrom, and H. Colfen, *Chem. Soc. Rev.* **43**, 2348 (2014).
  - [11] V. N. Novikov and A. P. Sokolov, *Nature* **431**, 961 (2004).
  - [12] S. Lan, C. Guo, W. Zhou, Y. Ren, J. Almer, C. Pei, H. Hahn, C.-T. Liu, T. Feng, X.-L. Wang, and H. Gleiter, *Commun. Phys.* **2**, 117 (2019).
  - [13] Z. Ye, F. Zhang, Y. Sun, M. I. Mendelev, R. T. Ott, E. Park, M. F. Besser, M. J. Kramer, Z. J. Ding, C. Z. Wang, and K. M. Ho, *Appl. Phys. Lett.* **106**, 101903 (2015).
  - [14] Z. Ye, F. Zhang, Y. Sun, M. C. Nguyen, S. H. Zhou, L. Zhou, F. Meng, R. T. Ott, E. Park, M. F. Besser, M. J. Kramer, Z. J. Ding, M. I. Mendelev, C. Z. Wang, R. E. Napolitano, and K. M. Ho, *Phys. Rev. Mater.* **1**, 055601 (2017).
  - [15] R. Busch, S. Schneider, A. Peker, and W. Johnson, *Appl. Phys. Lett.* **67**, 1544 (1995).
  - [16] J. C. Qiao, Q. Wang, J. M. Pelletier, H. Kato, R. Casalini, D. Crespo, E. Pineda, Y. Yao, and Y. Yang, *Prog. Mater. Sci.* **104**, 250 (2019).
  - [17] T. S. Ingebrigtsen, J. C. Dyre, T. B. Schroder, and C. P. Royall, *Phys. Rev. X* **9**, 031016 (2019).
  - [18] K. Kelton, *Philos. Mag. Lett.* **77**, 337 (1998).

- [19] H. W. Sheng, W. K. Luo, F. M. Alamgir, J. Bai, and E. Ma, *Nature* **439**, 419 (2006).
- [20] A. Hirata, P. Guan, T. Fujita, Y. Hirotsu, A. Inoue, A. R. Yavari, T. Sakurai, and M. Chen, *Nat. Mater.* **10**, 28 (2011).
- [21] D. Z. Chen, C. Y. Shi, Q. An, Q. Zeng, W. L. Mao, W. A. Goddard, and J. R. Greer, *Science* **349**, 1306 (2015).
- [22] J. Ding and E. Ma, *Npj Comput. Mater.* **3**, 9 (2017).
- [23] Z. Zhang and W. Kob, *Proc. Natl. Acad. Sci. USA* **117**, 14032 (2020).
- [24] L. Xing, T. Hufnagel, J. Eckert, W. Löser, and L. Schultz, *Appl. Phys. Lett.* **77**, 1970 (2000).
- [25] L. Xing, Y. Shen, and K. Kelton, *Appl. Phys. Lett.* **81**, 3371 (2002).
- [26] S. K. Das, J. H. Perepezko, R. I. Wu, and G. Wilde, *Mater. Sci. Eng.: A* **304–306**, 159 (2001).
- [27] J. Holzer and K. Kelton, *Acta Metall. Mater.* **39**, 1833 (1991).
- [28] C. Desgranges and J. Delhommelle, *Phys. Rev. Lett.* **120**, 115701 (2018).
- [29] J. Russo, F. Romano, and H. Tanaka, *Phys. Rev. X* **8**, 021040 (2018).
- [30] L. Battezzati, M. Baricco, P. Schumacher, W. C. Shih, and A. L. Greer, *Mater. Sci. Eng.: A* **179**, 600 (1994).
- [31] G. Wilde, H. Sieber, and J. H. Perepezko, *Scr. Mater.* **40**, 779 (1999).
- [32] Y. Sun, F. Zhang, Z. Ye, Y. Zhang, X. Fang, Z. Ding, C. Wang, M. I. Mendelev, R. T. Ott, and M. J. Kramer, *Sci. Rep.* **6**, 23734 (2016).
- [33] L. Wang, J. J. Hoyt, N. Wang, N. Provatas, and C. W. Sinclair, *Nat. Commun.* **11**, 724 (2020).
- [34] Materials Preparation Center at Ames Laboratory (USDOE), Ames, IA, USA, [www.mpc.ameslab.gov](http://www.mpc.ameslab.gov).
- [35] M. J. Kramer, H. Mecco, K. W. Dennis, E. Vargonova, R. W. Mccallum, and R. E. Napolitano, *J. Non-Cryst. Solids* **353**, 3633 (2007).
- [36] See Supplemental Material at <https://link.aps.org/supplemental/10.1103/PhysRevMaterials.5.043402> for the uniform amorphous nature, details of phase transformation sequence and atomic packing of metastable phases in Al-Sm ribbon.
- [37] W. M. Brown, P. Wang, S. J. Plimpton, and A. N. Tharrington, *Comput. Phys. Commun.* **182**, 898 (2011).
- [38] W. M. Brown, A. Kohlmeyer, S. J. Plimpton, and A. N. Tharrington, *Comput. Phys. Commun.* **183**, 449 (2012).
- [39] W. M. Brown and M. Yamada, *Comput. Phys. Commun.* **184**, 2785 (2013).
- [40] M. Mendelev, F. Zhang, Z. Ye, Y. Sun, M. Nguyen, S. Wilson, C. Wang, and K. Ho, *Modell. Simul. Mater. Sci. Eng.* **23**, 045013 (2015).
- [41] M. Finnis and J. Sinclair, *Philos. Mag. A* **50**, 45 (1984).
- [42] F. Zhang, M. I. Mendelev, Y. Zhang, C.-Z. Wang, M. J. Kramer, and K.-M. Ho, *Appl. Phys. Lett.* **104**, 061905 (2014).
- [43] Y. Sun, Y. Zhang, F. Zhang, Z. Ye, Z. Ding, C. Z. Wang, and K. M. Ho, *J. Appl. Phys.* **120**, 015901 (2016).
- [44] L. Zhou, F. Meng, S. Zhou, K. Sun, T.-H. Kim, R. T. Ott, R. E. Napolitano, and M. J. Kramer, *Acta Mater.* **164**, 697 (2019).
- [45] Y. E. Kalay, C. Yeager, L. S. Chumbley, M. J. Kramer, and I. E. Anderson, *J. Non-Cryst. Solids* **356**, 1416 (2010).
- [46] L. Yang, F. Zhang, F.-Q. Meng, L. Zhou, Y. Sun, X. Zhao, Z. Ye, M. J. Kramer, C.-Z. Wang, and K.-M. Ho, *Acta Mater.* **156**, 97 (2018).
- [47] B. Karpe, B. Kosec, and M. Bizjak, *J. Achiev. Mater. Manuf. Eng.* **51**, 59 (2012).
- [48] M. Sowjanya and T. K. K. Reddy, *J. Mater. Process. Technol.* **214**, 1861 (2014).
- [49] C. Xu, H. Wang, F. Qiu, Y. Yang, and Q. Jiang, *Mater. Sci. Eng.: A* **417**, 275 (2006).
- [50] J. H. He, H. W. Sheng, P. J. Schilling, C.-L. Chien, and E. Ma, *Phys. Rev. Lett.* **86**, 2826 (2001).
- [51] Y. Sun, S.-X. Peng, Q. Yang, F. Zhang, M.-H. Yang, C.-Z. Wang, K.-M. Ho, and H.-B. Yu, *Phys. Rev. Lett.* **123**, 105701 (2019).
- [52] X. W. Fang, C.-Z. Wang, Y. X. Yao, Z. J. Ding, and K.-M. Ho, *Phys. Rev. B* **82**, 184204 (2010).
- [53] P. M. Derlet and R. Maaß, *J. Alloys Compd.* **821**, 153209 (2020).
- [54] F. Mura and A. Zacccone, *Phys. Rev. E* **93**, 042803 (2016).
- [55] J. J. De Yoreo and P. G. Vekilov, *Rev. Mineral. Geochem.* **54**, 57 (2003).
- [56] A. Vuppuluri and S. Vedantam, *Philos. Mag. Lett.* **96**, 339 (2016).
- [57] V. Tikare, E. A. Holm, D. Fan, and L. Chen, *Acta Mater.* **47**, 363 (1998).



**Supplemental Material for**  
**“Unveiling the mechanism of phase and morphology selections during the**  
**devitrification of Al-Sm amorphous ribbon”**

Fanqiang Meng<sup>1\*</sup>, Yang Sun<sup>2,3\*</sup>, Feng Zhang<sup>2</sup>, Bo Da<sup>4</sup>, Cai-Zhuang. Wang<sup>2</sup>, Matthew J. Kramer<sup>2</sup>, Kai-Ming Ho<sup>2</sup>, Dongbai Sun<sup>1,5\*</sup>

<sup>1</sup>Sino-French Institute of Nuclear Engineering and Technology, Sun Yat-Sen University, Zhuhai, Guangdong, 519082, China

<sup>2</sup>Ames Laboratory, U.S. Department of Energy and Department of Physics, Iowa State University, Ames, Iowa 50011, USA

<sup>3</sup>Department of Applied Physics and Applied Mathematics, Columbia University, New York, New York 10027, USA

<sup>4</sup>Research and Services Division of Materials Data and Integrated System, National Institute for Materials Science, 1-1 Namiki, Tsukuba, Ibaraki 305-0044, Japan

<sup>5</sup>School of Materials, Sun Yat-Sen University, Guangzhou, Guangdong, 510275, China

Corresponding Authors: [\\*ys3339@columbia.edu](mailto:ys3339@columbia.edu) (Y.S.); [\\*sundongbai@mail.sysu.edu.cn](mailto:sundongbai@mail.sysu.edu.cn) (D.S.);  
[\\*mengfq5@mail.sysu.edu.cn](mailto:mengfq5@mail.sysu.edu.cn) (F.M.)

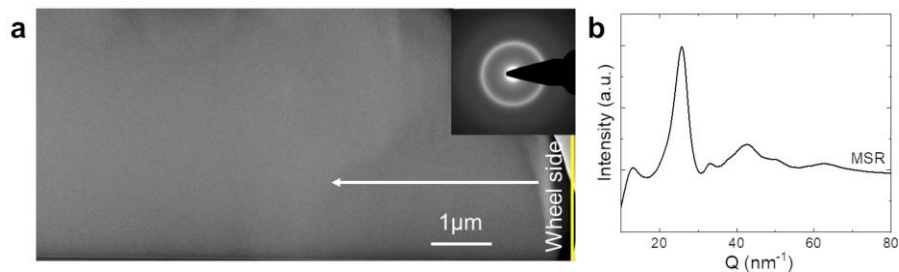


**Fig. S1** Amorphous nature of as-spun ribbon (a) TEM and corresponding SAD pattern demonstrate the homogeneous amorphous without any detectable nanocrystal, the wheel-side surface was labeled, and the arrow indicates the direction to free side; (b) HEXRD pattern without sharp crystalline peaks reveals the pure amorphous phase. Pre-peak and subpeak around  $Q=13$  and  $33 \text{ nm}^{-1}$  indicate the existence of short/medium-range ordering clusters.

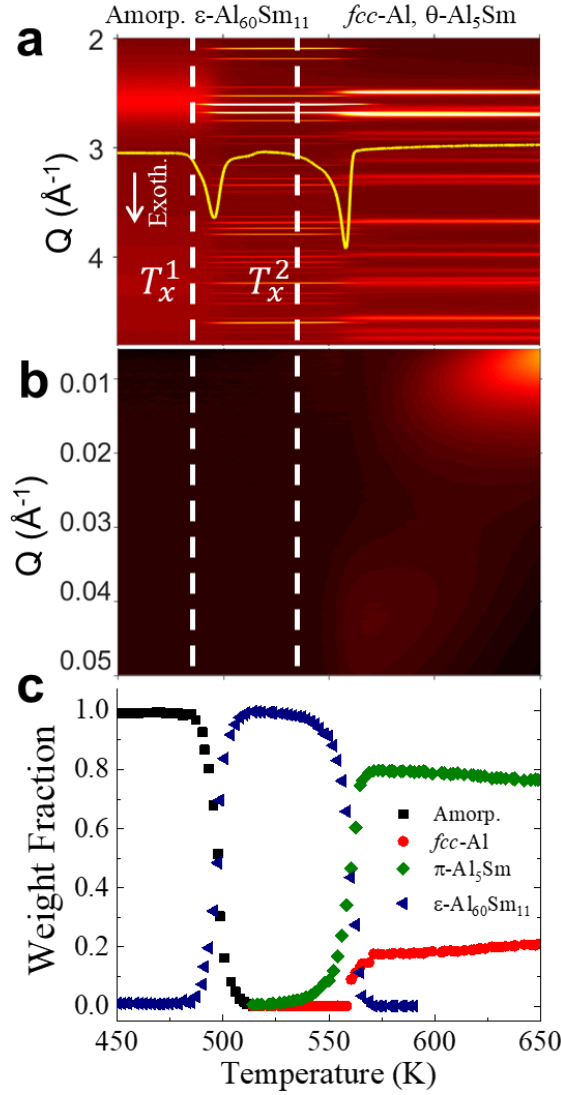


**Fig. S2** Phase transformation sequence of AlSm ribbon at a constant heating rate of 10K/min (a) WAXS, (b) SAXS, and (c) phase fraction evolution as a function of temperature, DSC profile is superimposed for comparison exothermic direction are labeled. Dashed lines denote onset temperatures for the first and second phase transformation. Rietveld analysis reveals the first exothermic peak is the corresponding formation of the  $\epsilon$ -Al<sub>60</sub>Sm<sub>11</sub>. Continuous heating up to 538 K leads to the decomposition of  $\epsilon$ -Al<sub>60</sub>Sm<sub>11</sub> into  $\pi$ -Al<sub>5</sub>Sm and *fcc*-Al. SAXS results in (b) shows that the initial crystallization from the amorphous phase to  $\epsilon$ -Al<sub>60</sub>Sm<sub>11</sub>, is in a partition-less manner. For temperatures above the onset temperature of the second exothermic event (538 K), a wide SAXS peak emerges at  $Q=0.042 \text{ \AA}^{-1}$ , characteristic length of 15 nm where  $L=2\pi/Q$ . The SAXS peak is related to the chemical fluctuations between *fcc*-Al and  $\pi$ -Al<sub>5</sub>Sm, from the decomposition of  $\epsilon$ -Al<sub>60</sub>Sm<sub>11</sub>. The intensity of the SAXS peak becomes more pronounced with increasing temperature, and the peak positions shift to a lower  $Q$ , indicating that both the volume fractions and average sizes of the *fcc*-Al and  $\pi$ -Al<sub>5</sub>Sm phases are increasing.



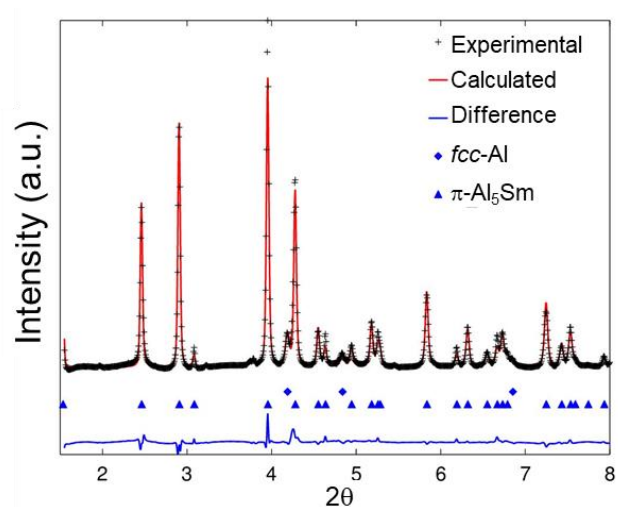


**Fig. S3** Phase configuration after the second exothermic peak. GSAS Rietveld result of the WAXS pattern at 600K, indicating the only existence of *fcc*-Al and  $\pi$ -Al<sub>5</sub>Sm.

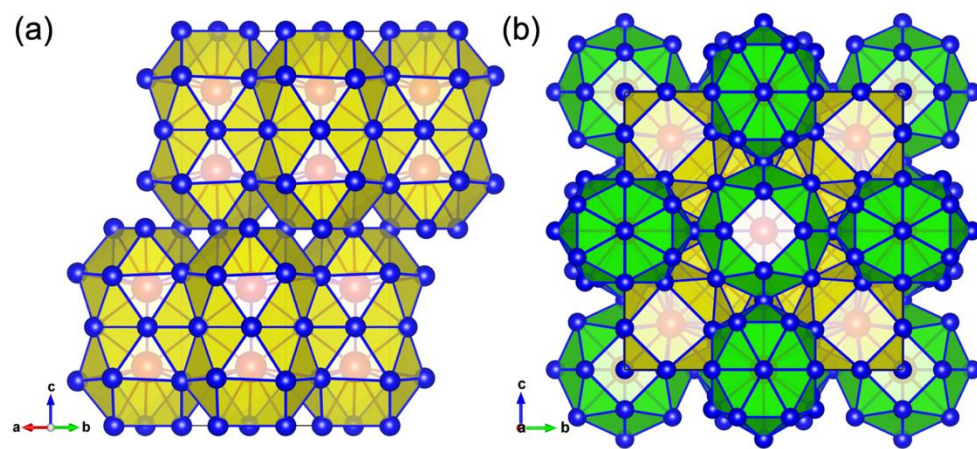


**Fig. S4** The packing of 3661 (yellow) and 16661 (green) clusters in the (a)  $\theta$ -Al<sub>5</sub>Sm and (b)  $\epsilon$ -Al<sub>60</sub>Sm<sub>11</sub> phase. Blue is Al, and Red is Sm.